A new route to achieve high strength and high ductility compositions in Cr-Co-Ni-based medium-entropy alloys: A predictive model connecting theoretical calculations and experimental measurements

AUTHOR(S):

Wang, Zhi; Li, Le; Chen, Zhenghao; Yuge, Koretaka; Kishida, Kyosuke; Inui, Haruyuki; Heilmaier, Martin

CITATION:

Wang, Zhi ...[et al]. A new route to achieve high strength and high ductility compositions in Cr-Co-Ni-based medium-entropy alloys: A predictive model connecting theoretical calculations and experimental measurements. Journal of Alloys and Compounds 2023, 959: 170555.

ISSUE DATE:

2023-10-10

URL:

http://hdl.handle.net/2433/282862

Journal of Alloys and Compounds 959 (2023) 170555

Contents lists available at ScienceDirect

Journal of Alloys and Compounds

journal homepage: www.elsevier.com/locate/jalcom

Research article

A new route to achieve high strength and high ductility compositions in Cr-Co-Ni-based medium-entropy alloys: A predictive model connecting theoretical calculations and experimental measurements

Zhi Wang [a], Le Li [a], Zhenghao Chen [a,*], Koretaka Yuge [a], Kyosuke Kishida [a], Haruyuki Inui [a], Martin Heilmaier [b]

[a] Department of Materials Science and Engineering, Kyoto University, Kyoto 606–8501, Japan
[b] Institute for Applied Materials (IAM-WK), Karlsruhe Institute of Technology (KIT), Engelbert-Arnold-Strasse 4, 76131 Karlsruhe, Germany

ARTICLE INFO

Article history:
Received 25 January 2023
Received in revised form 28 April 2023
Accepted 11 May 2023
Available online 12 May 2023

Keywords:
Metals and alloys
Mechanical properties
Dislocations and disclinations
Phase transitions
Computer simulations
Transmission electron microscopy

ABSTRACT

A new route to achieve high strength and high ductility compositions in the Cr-Co-Ni medium entropy alloys (MEAs) is proposed, by controlling the solid solution hardening parameter (Mean Square Atomic Displacement, MSAD) and twinning propensity parameter (Stacking Fault Energy, SFE), respectively. The MSAD is calculated to increase with the increase in the Cr content and with the increase in the Ni/Co ratio at high Cr concentrations, while the SFE is calculated to decrease with the increase in the Cr content and with the increase in the Co/Ni ratio at high Cr concentrations. In experiment, the strength at 0 K (derived from the temperature dependence of yield stress) increases as the Cr content increases and/or as the Ni content increases for a given high Cr content, so that a linear correlation is found between the yield strength at 0 K and MSAD. The SFE also decreases as the Cr content increases and as the Co content increases for a given high Cr content. However, while the tensile elongation increases with the decrease in SFE down to SFE values of 10–12 mJ/m^2, it abruptly decreases once the SFE decreases below this value due to a change in major deformation mode from deformation twinning to deformation-induced ε-martensite transformation. Based on the established connection between the theoretical calculation and experimental measurement, outstanding combinations of strength and ductility are predicted and experimentally confirmed at high Cr compositions and at a bit Ni-rich side of the Co/Ni equi-composition line. The proposed composition (around 45Cr-20Co-35Ni) exhibits a greater 0 K strength and a superior 77 K tensile ductility by 32 % and 13 %, respectively, compared to those of the equiatomic Cr-Co-Ni alloy.

1. Introduction

In recent years, there is a tremendous interest in high- and medium-entropy alloys (HEA and MEA) as a new class of alloy offering an excellent combination of high strength and high ductility. According to some systematic study under FCC (face-centered cubic) HEA in the Cr-Mn-Fe-Co-Ni system and MEAs in its subsystems, the high strength is believed to be related to severely distorted crystal lattice [1–9]. This might be due to the different atomic sizes of the constituent elements while the high ductility is attributed to the propensity of twinning (as well as ε-martensitic transformation) arising from the low stacking fault energies (SFEs) (in other words, the relative energy difference between FCC and HCP (hexagonal close-packed) phases) [10–15]. Many early studies on HEAs and MEAs were made on those alloys with equiatomic compositions (i.e., the equal fractions of the constituent elements). Of these equiatomic HEA and MEAs in the Cr-Mn-Fe-Co-Ni and its sub-systems, the Cr-Co-Ni MEA is known to exhibit the most excellent combination of high strength and high ductility [11,15–18]. Many recent studies are thus devoted to ternary Cr-Co-Ni MEAs rather than quinary Cr-Mn-Fe-Co-Ni HEAs, focusing on further improvement of strength and ductility through tuning the degree of short-range order [19–25], changing the chemical composition to deviate from the equiatomic to non-equiatomic ones [26–34] and so on. The approach to change the chemical composition to non-equiatomic ones seems reasonable and promising as the degree of lattice distortion and the relative stability of FCC and HCP phases would be largely varied in a wide FCC single-phase field in the Cr-Co-Ni ternary system.

However, it is not trivial to find out a proper composition range, where higher strength and higher ductility are simultaneously achieved, even though in the simplest ternary Cr-Co-Ni system. The trial-and-error type experiment approach suffers from a vast space of potential combinations of the constituent elements and is almost impossible to

* Corresponding author.
E-mail address: chen.zhenghao.6e@kyoto-u.ac.jp (Z. Chen).

https://doi.org/10.1016/j.jallcom.2023.170555

reach the proper composition in a finite period. Indeed, experimental efforts by Yoshida et al. [28] failed to find out a composition range to achieve strength and ductility simultaneously, superior to those of the equiatomic Cr-Co-Ni MEA. A theoretical predication approach is then urgently required to guide a proper composition range from a vast space of potential combinations of the constituent elements. Unfortunately, very limited efforts can be found for Cr-Co-Ni alloy design based on computational prediction, and the verification of the predictive reliability is not unambiguous. Coury et al. [26,27,34] utilized the solid solution hardening models proposed by Toda-Caraballo et al. [35] and Varvenne et al. [36] to predict the yield strength and the relative phase stability between FCC and HCP (SFE) to tailor the tensile ductility. Nevertheless, these studies are a little bit of sporadic and confusing so that one may suspect the viability of achieving superior strength and ductility simultaneously by changing compositions. For example, while they founded a composition of 45Cr-27.5Co-27.5Ni as the strongest alloy only from two non-equiatomic counterparts [26], the optimization of tensile ductility was achieved by another composition of 40Cr-55Co-5Ni [27]. Yang et al. [32] calculated the shear modulus and SFE as the critical indicator for strength and tensile ductility of Cr-Co-Ni alloy system, respectively and proposed the optimal composition region in Cr-Co-Ni system as 30–35 at. % Cr, 60–67 at. % Co, and 0–6 at. % Ni. This prediction somehow remains doubtful due to the absence of a convincing correlation between shear modulus and yield strength of FCC metals and alloys. In short, although the above studies have preliminarily explored the potential of theoretical predication-guided Cr-Co-Ni alloy design, it is still not easy to say which composition exhibits the best property at the moment and the bridge between the theoretical calculation and experiment is yet to be established.

In our previous work, we have proposed the mean square atomic displacement (MSAD) as the material parameter to quantify the lattice distortion and predict the yield strength of FCC HEA/MEAs of the Cr-Mn-Fe-Co-Ni system [1,8,9]. The MSAD parameter has been successfully used to design novel HEA/MEAs with superior strength [6,37–41]. In addition, the recent study on non-equiatomic Cr-Mn-Fe-Co-Ni HEAs has shown that the model based on MSAD parameter exhibits desire accuracy in predicting their strengths. On the other hand, the SFE has already been widely applied as a key factor to effectively deduce the proper composition for superior ductility by activating the twinning-induced plasticity (TWIP) and/or transformation-induced plasticity (TRIP) effect in FCC HEA/MEAs [9,11,27,30–32,34,38,42–46]. These results thus motivate us to adopt the MSAD and SFE as the predictive parameters aimed at superior strength and ductility in the Cr-Co-Ni alloy system.

To that end, in the present study, we utilize computational approach to make predictions on the strength and ductility in Cr-Co-Ni based alloys and make a systematic investigation in validating the predictive reliability by experimental work. The MSAD as well as the SFE values of non-equiatomic Cr-Co-Ni alloys with fcc single phase structures in the present study are theoretically calculated by density functional theory, and subsequently the mechanical properties of candidate compositions with higher MSAD and/or lower SFE values (preferred to superior strength and/or ductility, respectively) are investigated with polycrystal specimens. We discuss the correlation between the calculated MSAD value and the strength (yield stress), and between the calculated SFE value and the ductility (elongation) based on experimental results. We propose a proper composition range in Cr-Co-Ni ternary system which is expected to exhibit simultaneous high strength and high ductility.

2. Methods and materials

2.1. Computational methods

Computations of MSAD and SFE values were carried out based on first-principles total energy calculations using the Vienna ab initio simulation package (VASP) [47,48]. Special quasirandom structure (SQSs) [49–51] were constructed by performing a simulated annealing-based algorithm [52] to optimize the configurations by minimizing residuals of the correlation functions between configurations and the randomized state, from the first to sixth nearest neighbor pairs for bulk calculation of MSAD values, and the first to fourth nearest neighbor pairs for slab calculation of SFE values. 18 and 12 correlation functions in total were taken into consideration, respectively. Finally, we constructed optimized SQSs containing 108 atoms with a 3×3x3 expansion of FCC unit cell for MSAD calculation and those containing 216 atoms with 6-layer (111) close-packed atomic planes for SFE calculation, respectively. For the first-principles total energy calculation, the projector augmented wave (PAW) [53] method was employed within the generalized gradient approximation (GGA) parameterized by Perdew and Wang [54]. Brillouin-zone integration was performed using the Methfessel-Paxton method, using Monkhorst-Pack *k*-point meshes and a smearing parameter of 0.1 eV [55,56]. The cutoff energy of the plane wave was set to 450 eV in this work. Total energies were minimized until $1 \times 10^{-5} eV$ between successive steps, while cell shape and cell volume were fixed with internal atomic positions relaxed until the residual forces became less than $1 \times 10^{-3} eV/Å$. For each alloy composition, we took the arithmetic mean value of calculation results from 12 input SQSs for the MSAD value and those from 6 input SQSs for the SFE value, respectively.

For MSAD computations, after relaxation, the theoretical lattice parameter corresponding to the minimized ground state total energy was calculated and the average MSAD values together with MSAD values for each of the constituent elements were derived.

For SFE computations, the correlation functions near the stacking fault interfaces were intendedly checked during the optimization process to ensure the randomness near interfaces. A vacuum layer with thickness of 1.2 nm was introduced between stacking sequences to ensure the 2D periodic boundary condition (PBC) and reduce interactions between slabs. Then, an intrinsic stacking fault was introduced to SQSs by shifting the top 3 layers with respect to

Table 1
Averaged VEC, theoretically calculated MSAD and SFE and experimentally determined SFE of nine different non-equiatomic and equiatomic Cr-Co-Ni ternary alloys.

	VEC	MSAD ($\mathbf{pm^2}$)	γ_{isf} ($\mathbf{mJ/m^2}$)	SFEexp ($\mathbf{mJ/m^2}$)	Microstructure after cold rolling	Microstructure after recrystallization
50Cr-10Co-40Ni	7.9	89.07	-35.85 (−49.60 ~ −19.85)	-	-	fcc+bcc (Not Good)
50Cr-15Co-35Ni	7.85	81.64	-50.60 (−74.14 ~ −29.78)	-	-	fcc+bcc (Not Good)
45Cr-15Co-40Ni	8.05	56.56	-0.29 (−26.29 ~ 31.20)	21.5	fcc	fcc
45Cr-20Co-35Ni	8	51.63	-79.84 (−105.75 ~ −43.25)	15	fcc	fcc
45Cr-25Co-30Ni	7.95	49.52	-140.00 (−160.27 ~ −126.36)	10	fcc+hcp	fcc
40Cr-20Co-40Ni	8.2	40.46	-61.49 (−95.58 ~ −18.16)	-	fcc	fcc
40Cr-25Co-35Ni	8.15	37.14	-70.33 (−90.50 ~ −55.74)	-	fcc	fcc
40Cr-40Co-20Ni	8	35.53	-151.87 (−155.08 ~ −150.16)	-	fcc+hcp	fcc
40Cr-50Co-10Ni	7.9	34.83	-130.07 (−153.31 ~ −111.50)	-	fcc+hcp	fcc+hcp (Not Good)
33Cr-33Co-33Ni	8.33	28.56	-57.22 (−84.85 ~ −30.55)	14[23]	fcc	fcc

Table 2
Summary of experimentally-determined mechanical properties of six different non-equiatomic and equiatomic Cr-Co-Ni ternary alloys with FCC single phase structure.

	Grain size (μm)	Yield Stress at 0 K (MPa)	Yield Stress at RT (MPa)	UTS at RT (MPa)	Tensile Ductility at RT (%)	Uniform elongation at RT (%)	Yield Stress at 77 K (MPa)	UTS at 77 K (MPa)	Tensile Ductility at 77 K (%)	Uniform elongation at 77 K (%)
45Cr-15Co-40Ni	84.9	690	258.47	607.24	118.63	90.90	435.59	926.41	134.59	114.05
45Cr-20Co-35Ni	76.6	672	243.15	566.70	148.44	105.43	471.10	998.16	170.94	149.91
45Cr-25Co-30Ni	50.6	579	220.47	623.43	145.55	117.60	471.91	908.29	153.96	134.26
40Cr-20Co-40Ni	80.3	-	217.77	617.61	160.35	129.99	428.18	939.18	161.71	129.11
40Cr-25Co-35Ni	70.1	-	232.46	646.97	142.42	115.14	410.59	985.48	163.41	132.49
40Cr-40Co-20Ni	55.3	-	163.87	464.25	34.80	28.8	337.65	777.28	59.44	42.16
33Cr-33Co-33Ni	70.8	508	211.13	619.94	136.92	112.76	374.31	998.87	154.68	131.61

the bottom 3 layers by the Burgers vector ($\boldsymbol{b}_s$ =a/6 < 11$\bar{2}$ > where a is the lattice parameter) of the Shockley partial dislocation. Geometrical relaxation was applied to the layers near the interface with the same lattice parameters obtained in MSAD calculations. The SFE value was then derived as the residual energy between two cells normalized to the area of the stacking fault.

2.2. Experimental methods

Nine different Cr-Co-Ni alloys with non-equiatomic compositions as listed in Table 1 as well as the equiatomic Cr-Co-Ni alloy were prepared by arc-melting high-purity (> 99.9 %) Cr, Co, and Ni in an Ar atmosphere. These non-equiatomic compositions were selected based on the calculation results of MSAD and SFE values. Arc-melted ingots were homogenized at 1473 K for 168 h, followed by water-quenching. The alloys were cold-rolled to 40 % reduction in thickness and annealed at 1473 K for 15 min to obtain fully recrystallized structures. Microstructures for these alloys are listed in Table 1. Mechanical tests are not conducted for those alloys without a FCC single phase structure after the recrystallization process, that is, 50Cr-10Co-40Ni, 50Cr-15Co-35Ni and 40Cr-50Co-10Ni alloys. The remained six alloys exhibit the desired FCC single phase structure and have similar grain sizes in the range of 70–85 μm (Table 2) as measured by the (linear) intercept method (without counting annealing twin boundaries), except for 45Cr-25Co-30Ni and 40Cr-40Co-20Ni alloys. These latter two alloys exhibit a smaller grain size of 50–55 μm, the reason for which will be described later in Section 3.2.1. Specimens for tensile and compression tests with a gauge dimension of 2×2x5 mm^3 were prepared by electrical discharge machining. The specimen surface was mechanically and then electrolytically polished in a solution of 1:4 nitric acid and methanol by volume prior to mechanical testing. Compression tests were conducted on an Instron-type testing machine in the low temperature range from 10 K to room temperature at an initial strain rate of 1×10^{-4} s^{-1} to deduce the temperature dependence of yield stress, that is, the strength property. Tensile tests were also conducted on an Instron-type testing machine at an initial strain rate of 1×10^{-4} s^{-1} to observe the stress-strain behavior up to failure, that is, the ductility property. Unlike the compression tests, tensile properties were only investigated at two selected temperatures: the room temperature and 77 K (by immersing specimen in liquid nitrogen) due to the instrumental restriction. Mechanical tests for each condition were independently repeated by at least 3 specimens to reduce the experimental uncertainties. Details of the tensile tests are described in the supplementary material S1. After deformation, the specimen surface was again mechanically and electrolytically polished in the solution of nitric acid and methanol (1:4 by volume). Microstructures before and after deformation were examined by optical microscopy (OM) and scanning electron microscope (SEM) equipped with electron back-scatter diffraction (EBSD) and energy-dispersive X-ray spectroscopy (EDS) systems. Thin foils parallel to (111) slip planes were prepared by electro-polishing with a solution of nitric acid and methanol (1:2:7 by volume). Dislocation structures were examined by transmission electron microscopy (TEM) with a JEOL JEM-2000FX electron microscope operated at 200 kV.

3. Results

3.1. MSAD and SFE calculations

MSAD and SFE values calculated for some selected chemical compositions are depicted in Fig. 1(a) and (b), respectively, in the form of contour plots on the corresponding ternary phase diagram. The dotted line in the phase diagram indicates the boundary of the FCC single-phase field computationally determined at 1200 °C [57]. The calculated MSAD and SFE values are listed in Table 1 for some

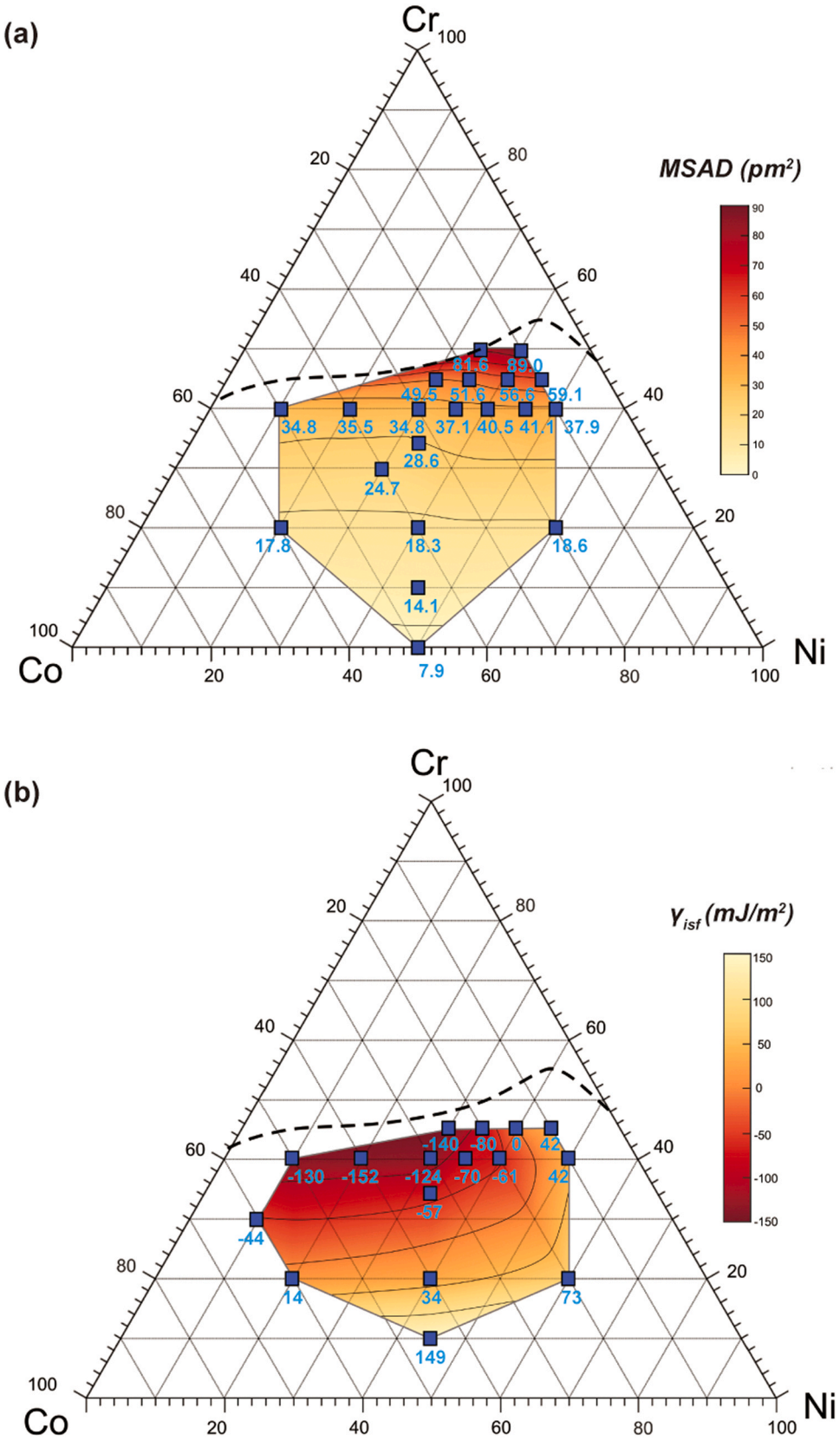

Fig. 1. Contour plots of (a) MSAD and (b) SFE values theoretically-calculated as a function of composition in the Cr-Co-Ni ternary system.

selected chemical compositions. As SFEs depend on the SQS employed, the range of SFEs is tabulated in Table 1 together with the averaged values. As expected, the MSAD value tends to increase with the increase in the Cr content, but the MSAD increase does not occur symmetrically with respect to the Co/Ni equi-composition line, especially at the higher Cr compositions. This leads to the maximum of MSAD occurring on the Ni-rich side of the Co/Ni equi-composition line for high Cr compositions, such as 45Cr-20Co-35Ni. The

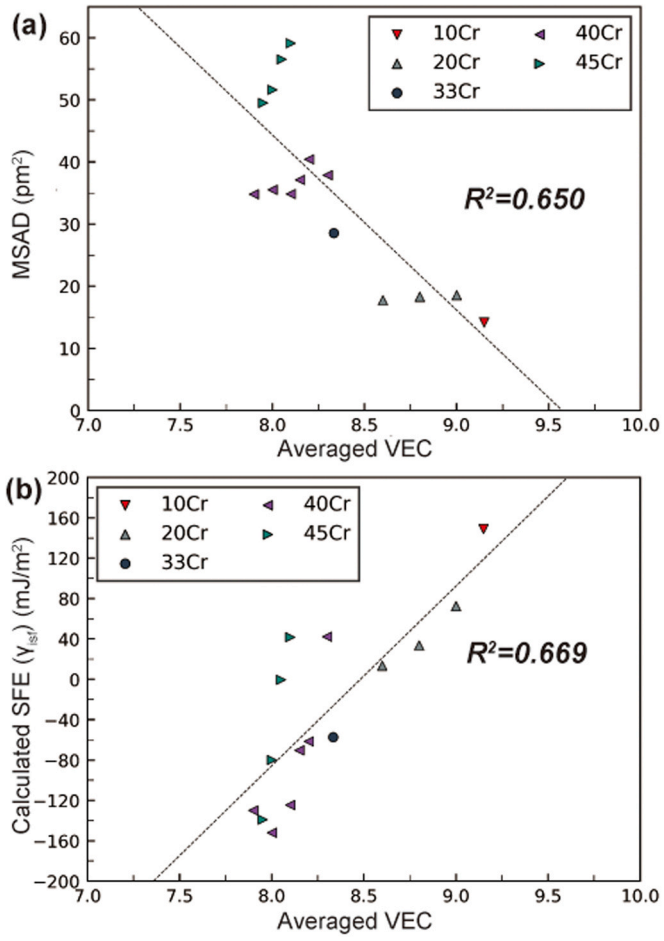

Fig. 2. Theoretically-calculated (a) MSAD and (b) SFE values of Cr-Co-Ni ternary alloys plotted as a function of VEC.

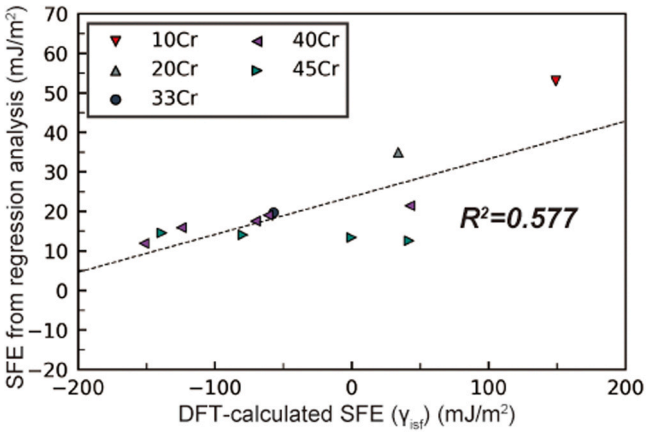

Fig. 3. SFE of Cr-Co-Ni ternary alloys deduced by regression analysis by Bertoli et al. [34] plotted as a function of SFE theoretically-calculated in the present study.

maximum strength is predicted to occur in the vicinity of such compositions on the assumption that the MSAD value correlates positively with the strength (at 0 K) [1,5,8,9]. This is a bit different from the strength prediction based on atomic size misfit by Coury et al. [26] who predicted the maximum strength occurs on the Co-rich rich side of the Co/Ni equi-composition line at the high Cr compositions.

As reported frequently in many previous papers, the SFE is negative for alloys with Cr contents of more than 30 % [17,20,58–60]. The SFE value tends to decrease with the increase in the Cr content with a more significant decrease occurring on the Co-rich rich side of the Co/Ni equi-composition line. This leads to the minimum of SFE occurring on the Co-rich side of the Co/Ni equi-composition line at high Cr compositions, such as 40Cr-40Co-20Ni. This is qualitatively consistent with the experimental result by Köster et al. [61] and the regression analysis by Bertoli et al. [62]. The calculated negative SFE represents a relative instability of the FCC phase that the HCP type (…abab…) stacking sequence is expected as more stable than that of the FCC type (…abca…) at 0 K. Although the physical meaning of the absolute value of the negative SFE is not clear, this value is able to be used as an index to predict the actual SFE, as reported by Ritchie et al. [20]. Indeed, a linear correlation between the calculated and experimental measured SFE values is confirmed in the present study, as shown in Section 3.2.4. In short, these calculations predict that the higher Cr (more than 40 %) is mandatory for high strength and high ductility and that at such high Cr contents, Ni-rich compositions are preferred for higher strength and Co-rich compositions for higher ductility.

The calculated MSAD and SFE values are plotted in Fig. 2(a) and (b), respectively, as a function of averaged valence electron concentration (VEC) of the relevant alloys. Symbols in the plots are changed depending on the Cr content, and for a given Cr content, alloys of higher Co/Ni ratios are plotted at lower VEC values. Although the scatter is not small (the quality of fit R^2 =0.669 and 0.650 respectively for Fig. 2(a) and (b)), the VEC value seems to be an appropriate scaling factor for both MSAD and SFE values for Cr-Co-Ni system. It is important to note, however, that the scaling of MSAD with VEC provides only a rough estimate, especially at high Cr contents. As seen in Fig. 2(a), the MSAD-VEC trend at a given high Cr content (such as 45Cr) is simply opposite to the overall MSAD-VEC trend. The scaling of SFE with VEC does not suffer from such a problem as seen in Fig. 2(b). Although SFE of binary Cu- and Ag-alloys is known to be negatively correlated with the electron concentration (the so-called e/a ratio) [63], a positive SFE-VEC correlation is roughly obtained in the present Cr-Co-Ni alloy system. Bertoli et al. [34] made a regression analysis for SFE of 30 experimental measurements and proposed a regression equation to express the SFE of the alloys in the Cr-Co-Ni system with chemical compositions (the atomic fractions of Cr (X_{Cr}) and Co (.)), as follows,

$$\mathrm{SFE(mJ/m^2)} = 248 - 835X_{Cr} - 323X_{Co} + 682X_{Cr}^2 - 39X_{Co}^2 + 777X_{Cr}X_{Co} \quad (1)$$

Unlike in DFT calculations, the SFE estimated with the regression Eq. (1) will never be negative, as experimentally determined SFE values (mostly by TEM observations at room temperature), from which the regression analysis was made, are always positive. However, there is a nice positive correlation between the SFEs estimated with (1) and those calculated in the present study, as shown in Fig. 3, indicating the effectiveness of DFT-calculated SFEs in the prediction of mechanical properties of MEAs in the Cr-Co-Ni system.

3.2. Deformation in tension and compression

3.2.1. Microstructure before mechanical testing

Based on the calculation results of MSAD and SFE, we prepared some non-equiatomic Cr-Co-Ni alloys (50Cr, 45Cr and 40 Cr series) together with the equiatomic alloy as shown in Tables 1 and 2. Except for 45Cr-25Co-30Ni and 40Cr-40Co-20Ni alloys, all 45Cr and 40Cr series are confirmed to exhibit a FCC single-phase microstructure (no secondary precipitated phase in grains or on grain boundaries) with similar grain sizes in the range of 70–85 μm (Table 2) after recrystallization at 1473 K (Fig. 4). The grain sizes of most alloys used in the present study are a bit larger than those (30–50 μm) usually used by other researchers [26,27,33,34].

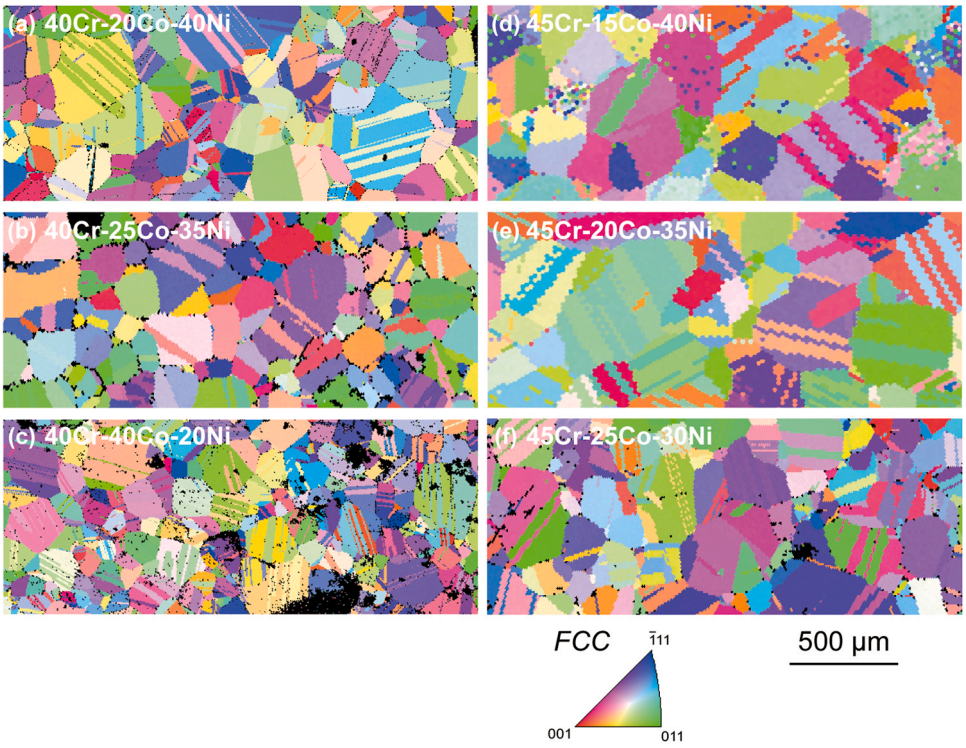

Fig. 4. Orientation Maps of (a) 40Cr-20Co-40Ni, (b) 40Cr-25Co-35Cr, (c) 40Cr-40Co-20Cr, (d) 45Cr-15Co-40Ni, (e) 45Cr-20Co-35Ni and (f) 45Cr-25Co-30Ni alloys after cold-rolling to 40 % reduction and subsequent annealing at 1473 K for 15 min.

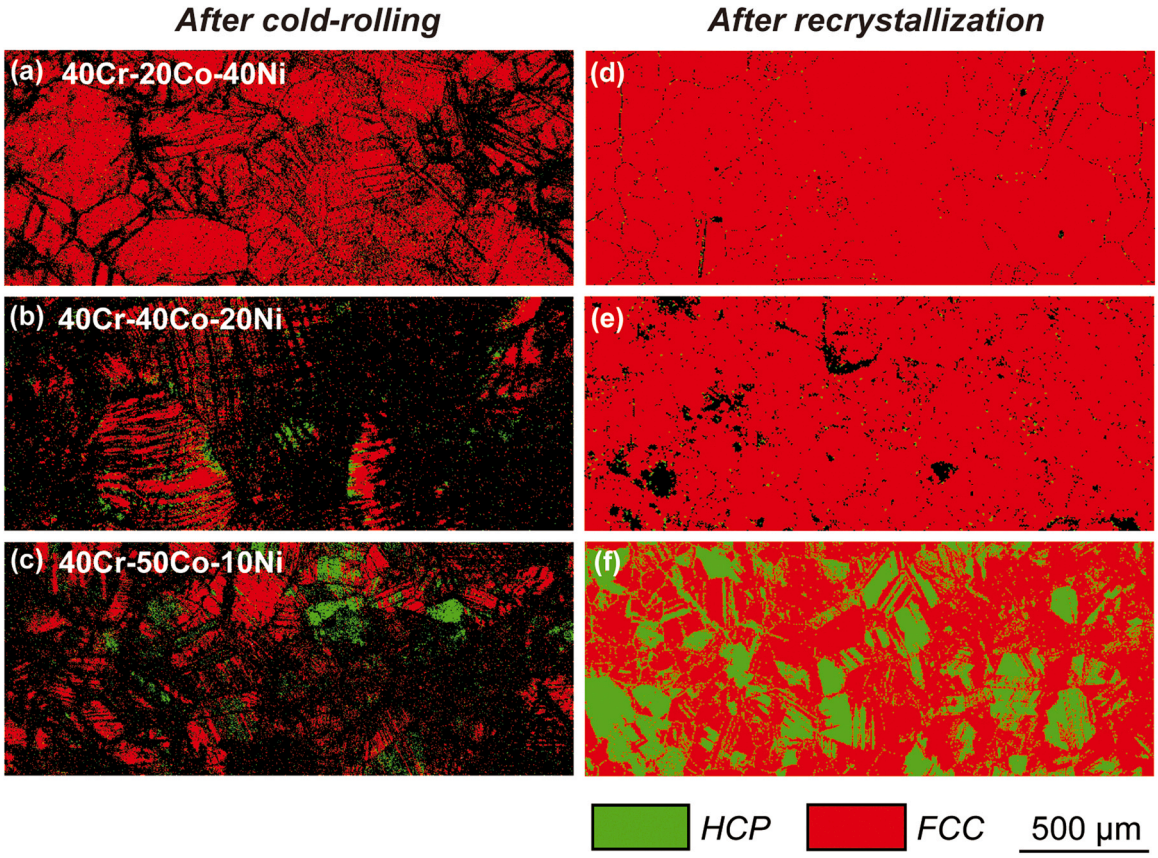

Fig. 5. Phase (FCC and HCP) maps (a)-(c) after cold-rolling to 40 % reduction and (d)-(f) after subsequent annealing at 1473 K for 15 min for (a), (d) 40Cr-20Co-40 Ni, (b), (e) 40Cr-40Co-20Ni and (c), (f) 40Cr-50Co-10Ni alloys.

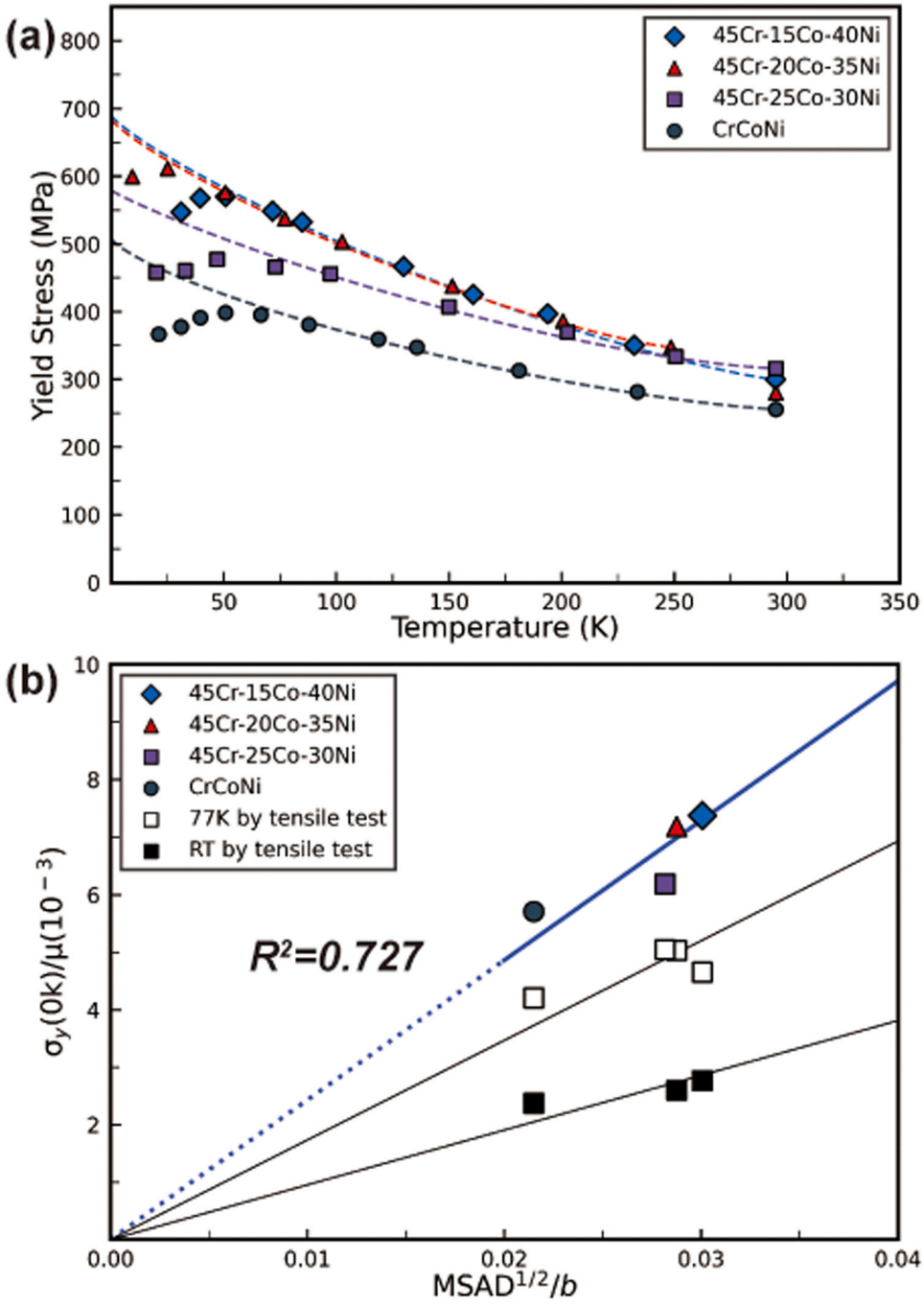

Fig. 6. Strength properties of investigated alloys. (a) Temperature dependence of yield stress for three alloys of the 45Cr series and the equiatomic Cr-Co-Ni alloys obtained in compression and (b) the extrapolated 0 K yield stresses (normalized to their shear moduli) plotted as a function of square root of MSAD (normalized to the Burgers vector). For comparison, similar plots are made also for the yield stress obtained in tension at 77 K and room temperature.

Consequently, the yield strengths obtained in the present study are expected to be lower than those obtained by other researchers for alloys of the same chemistry in view of grain boundary strengthening. The 45Cr-25Co-30Ni and 40Cr-40Co-20Ni alloys exhibit a smaller grain size of 50–55 μm. This is in essence because of the introduction of deformation-induced HCP laths during cold-rolling, as we confirmed that the microstructure of these two alloys before cold rolling is of the fcc single phase by EBSD and XRD analyses (Fig. 5(b) and S2). As the 45Cr-25Co-30Ni and 40Cr-40Co-20Ni alloys exhibit essentially a FCC single-phase microstructure after recrystallization at 1473 K, they were subjected to further characterization of mechanical properties. However, the 40Cr-50Co-10Ni alloy exhibits a FCC+HCP two-phase microstructure not only after cold-rolling (Fig. 5(c)) but also after recrystallization at 1473 K (Fig. 5(f)) Thus, the mechanical properties of this alloy were not determined. Moreover, Cr-rich precipitates with BCC structure are confirmed in high-Cr components (50Cr series), 50Cr-10Co-40Ni and 50Cr-15Co-35Ni alloys. These two alloys are hence also not supplied to further investigations.

3.2.2. Yield strength at 0 K

Fig. 6(a) shows yield stresses (defined as 0.2 % offset stress) plotted as a function of temperature obtained in compression for three different non-equiatomic alloys of the 45 Cr series and for the

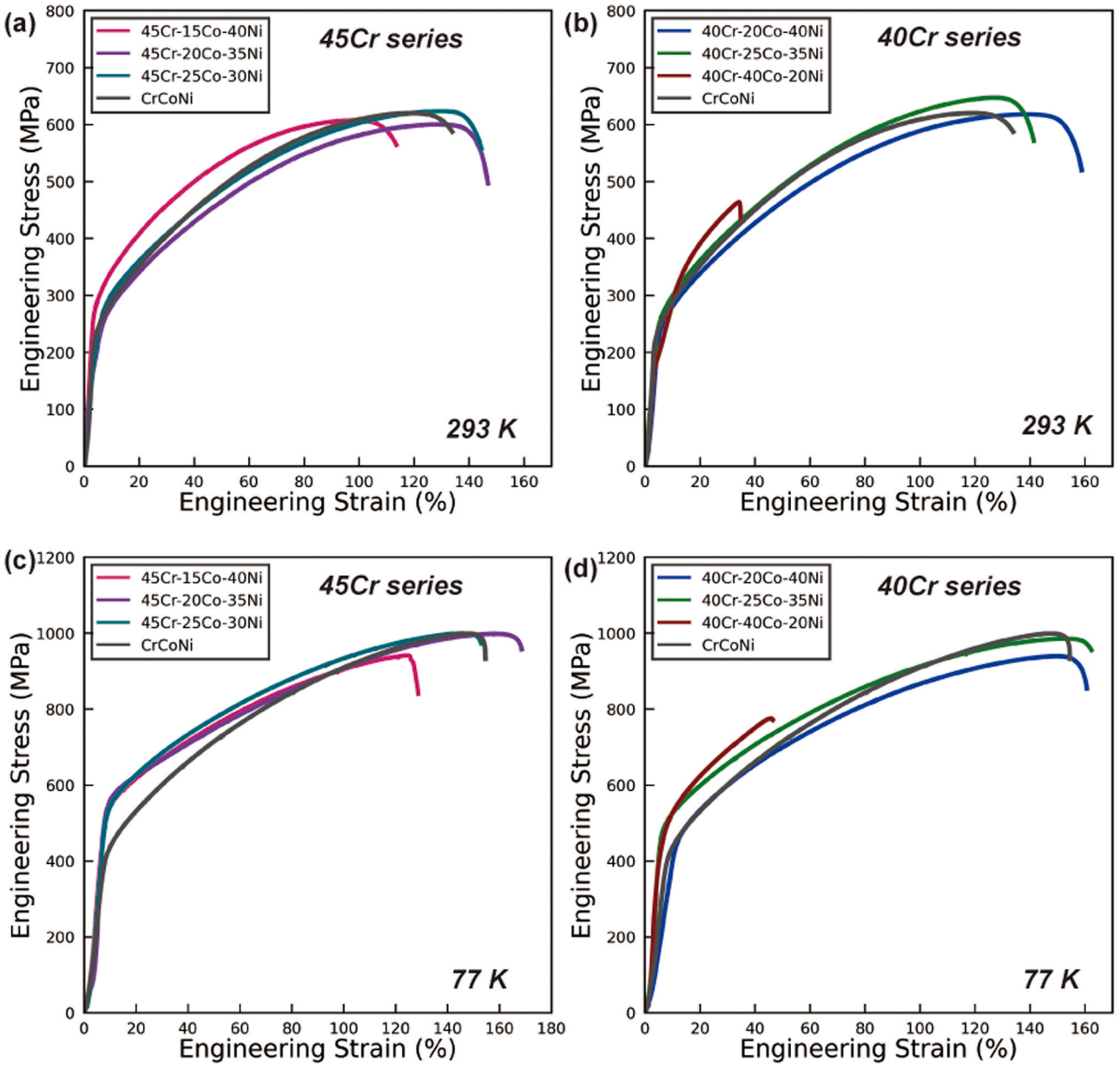

Fig. 7. Engineering strain-stress curves for (a), (c) alloys of the 45Cr series and (b), (d) those of the 40Cr series obtained at (a), (b) room temperature and (c), (d) 77 K.

equiatomic alloy. All alloys exhibit a significant temperature dependence of yield stress below room temperature. It is important to note that the extent of the temperature dependence of yield stress varies from alloy to alloy. For example, while three alloys of the 45 Cr series (45Cr-15Co-40Ni, 45Cr-20Co-35Ni and 45Cr-25Co-30Ni) exhibit similar yield stresses at room temperature, the 45Cr-25Co-30Ni alloy yields a smaller yield stress at lower temperatures. This indicates that the room-temperature yield stress cannot be a representative value of strength predicted by computational methods. For all alloys, the temperature dependence of yield stress becomes less significant below 77 K because of dislocation inertial effect, resulting in a dulling of the increase or even the decrease of the yield stress with the decreasing temperature. The inertial effect leads to a deviation of the thermal activated process of solid solution hardening and is supposed to be ignored when fitting the temperature dependence of yield stress [15]. The values of yield strength extrapolated to 0 K are then deduced by fitting their temperature dependencies above 77 K with an exponential function in the form of $\sigma_Y(T) = \sigma_{athermal} + \sigma_{thermal} \cdot \exp(-T/C)$, where T is the absolute temperature and C is a fitting parameter. The values of yield strength at 0 K deduced in such a way are tabulated in Table 2 and are plotted in Fig. 6(b) as a function of MSAD calculated in the present study. In Fig. 6(b), the yield strength at 0 K (σ_Y (0 K)) and MSAD are normalized to the shear modulus (μ) and Burgers vector ((b=a/$\sqrt{2}$), respectively. The shear modulus was estimated on the basis of Vegard's law with μ = 115, 76 and 76 GPa for Cr, Co and Ni, and the lattice constants were obtained by the DFT calculation as described in Section 2. A linear correlation is obviously observed in Fig. 6(b) between the yield strength at 0 K and MSAD. This clearly indicates that the MSAD value can be used to predict the strength of non-equiatomic alloys in the Cr-Co-Ni system, as in many quinary, quaternary and ternary equiatomic HEA and MEAs [1,8]. One point to note is that the strength at 0 K increases as the Ni content increases for the given 45Cr content. This is completely opposite to what is predicted for strength (the strength increases with the Co content) by Yoshida et al. [28].

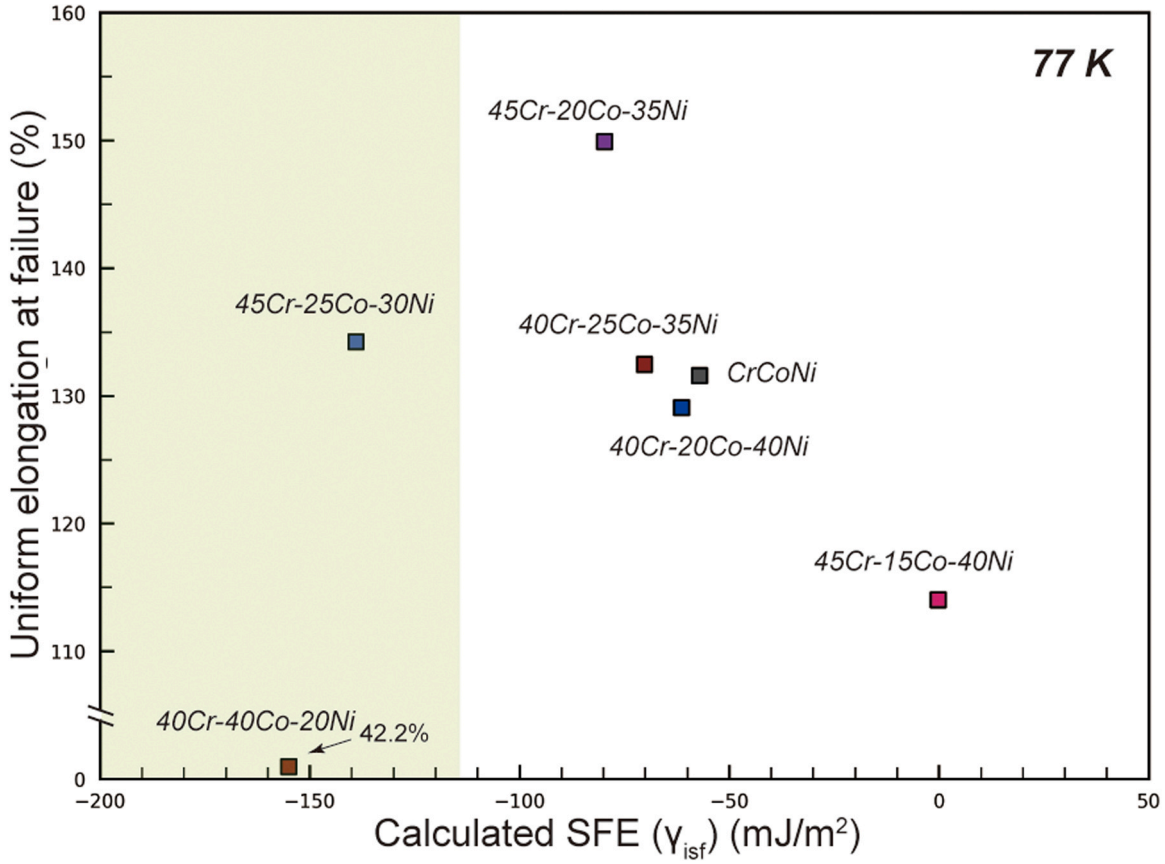

Fig. 8. Uniform elongation obtained for some selected Cr-Co-Ni ternary alloys in tension at 77 K plotted as a function of SFE theoretically calculated in the present study.

3.2.3. Tensile deformation behavior at 77 K and room temperature

Engineering stress-strain curves obtained in tension at 77 K and room temperature for non-equiatomic Cr-Co-Ni alloys (45Cr and 40Cr series) and the equiatomic alloy are shown in Fig. 7. Values of yield stress, ultimate tensile strength (UTS) and elongation at failure are tabulated in Table 2. The yield stress values deduced from the tensile test are well consistent to those deduced from the compression test, indicating no tension-compression asymmetry on the strength property. At room temperature, while the increase in yield stress for three alloys of the 40Cr series is not significant (by about 6–7 %) when compared to the equiatomic alloy, it is as high as 25–30 % for three alloys of the 45Cr series. At 77 K, all alloys of the 40Cr and 45Cr series exhibit significant increase in yield stress when compared to the corresponding values at room temperature. The increase in yield stress is more significant for alloys of the 40Cr series (by 85–90 %) than for alloys of the 45 series (by 65–70 %). This leads to the increase in 77 K yield stress by 10–15 and 20–25 % respectively for alloys of the 40Cr and 45Cr when compared to the equiatomic alloy. The variation of yield stress with alloys at the finite temperatures can be also scaled with the MSAD as shown in Fig. 6(b), although the MSAD scaling is originally proposed for the strength at 0 K [1].

On the other hand, the tensile ductility (i.e., elongation at failure) varies from alloy to alloy in a much more complex way instead of simply expected from the SFE values. Both at room temperature (Fig. 7(b)) and 77 K (Fig. 7(d)), the tensile ductility for 40Cr-20Co-40Ni and 40Cr-25Co-35Ni alloys is a little higher than that for the equiatomic alloy, probably due to their lower SFEs. Of interest to note is that although the 40Cr-40Co-20Ni alloy has a SFE lower than the equiatomic alloy, the tensile ductility is much lower. On the other hand, two alloys (45Cr-20Co-35Ni and 45Cr-25Co-30Ni) of the 45Cr series exhibit tensile ductility at 77 K and room temperature as expected from their SFEs; their tensile ductility is higher than that for the equiatomic alloy as their SFEs are lower than the equiatomic alloy. The 45Cr-15Co-40Ni alloy having a higher SFE than the equiatomic alloy exhibits a lower tensile ductility. The elongations at failure obtained at 77 K for these non-equiatomic and equiatomic alloys are plotted in Fig. 8 as a function of SFE calculated in the present study. The elongations at failure are seen to increase with the decrease in SFE down to a value of − 110 to − 120 mJ/m^2, but once the SFE decreases below this value, the tensile elongation at failure abruptly decreases. Some possible reasons for this will be rationalized by investigating deformation microstructures, see next section.

3.2.4. Deformation microstructures

Dislocation structures revealed by bright-field and weak-beam dark-field imaging are shown in Fig. 9(a), (b), (d), (e) and (g), (h), respectively, for 45Cr-15Co-40Ni, 45Cr-20Co-35Ni and 45Cr-25Co-30Ni alloys deformed to ~ 3 % plastic strain in compression at room temperature. The thin foils used were cut parallel to the (111) macroscopic slip plane. For all alloys, a typical planar array of smoothly curved long dislocations is observed on the (111) slip planes in the bright-field images of Fig. 9(a), (d), (g) and dislocations are observed to dissociate into two Shockley partial dislocations in the weak-beam images of Fig. 9(b), (e) and (h). The separation distance between paired Shockley partial dislocations was measured as a function of angle θ between the Burgers vector and line direction of the perfect dislocations in Fig. 9(c), (f) and (i) to deduce the stacking fault energy of these alloys. The deduced SFEs are 21.5, 15 and 10 mJ/m^2 for 45Cr-15Co-40Ni, 45Cr-20Co-35Ni and 45Cr-25Co-30Ni alloys,

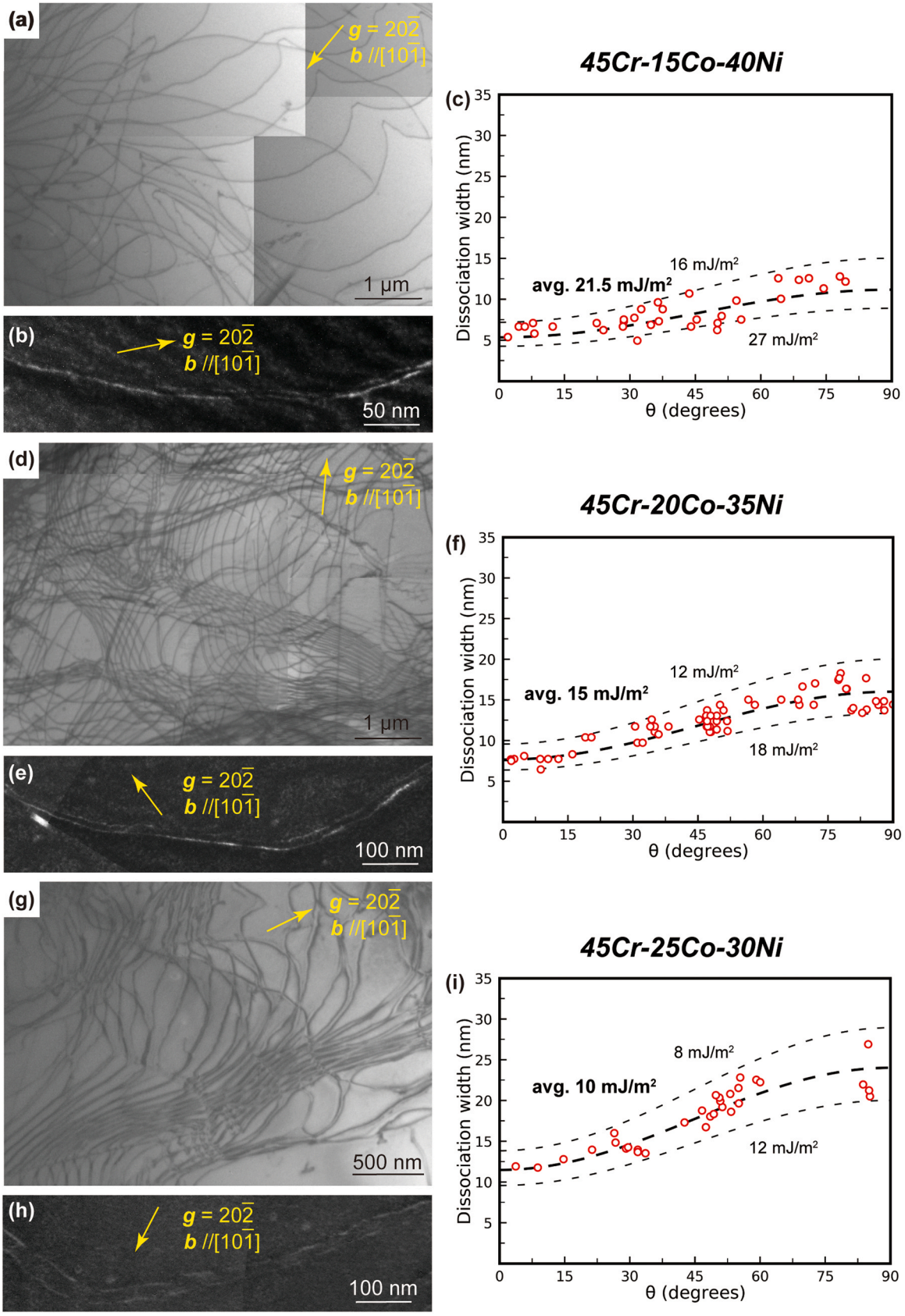

Fig. 9. Dislocation structures investigated by TEM after 3 % plastic deformation at room temperature. (a), (d), (g) Bright-field and (b), (e), (h) weak-beam dark-field TEM images of deformation microstructures at room temperature of (a), (b) 45Cr-15Co-40Ni, (d), (e) 45Cr-20Co-35Ni and (g), (h) 45Cr-25Co-30Ni alloys. (c), (f) and (i) Dissociation width plotted as a function of angle θ between the Burgers vector and line direction of the perfect dislocations for 45Cr-15Co-40Ni, 45Cr-20Co-35Ni and 45Cr-25Co-30Ni alloys, respectively.

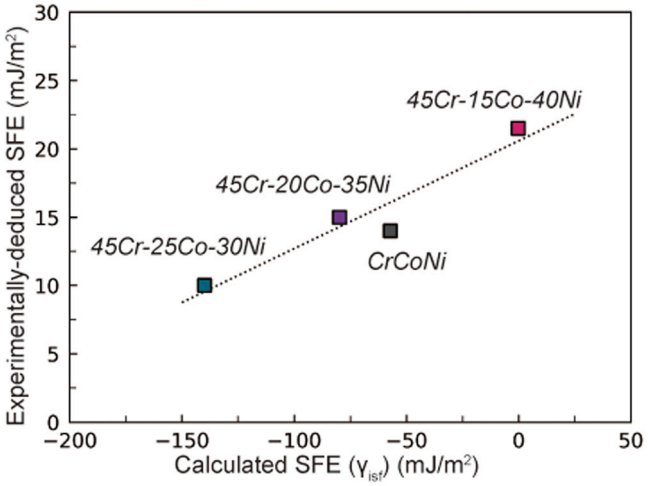

Fig. 10. SFEs experimentally determined by TEM analysis for 45Cr-15Co-40Ni, 45Cr-20Co-35Ni and 45Cr-25Co-30Ni alloys plotted as a function of SFEs theoretically calculated in the present study.

respectively. While the SFE for the 45Cr-20Co-35Ni alloy is comparable to that of the equiatomic Cr-Co-Ni alloy (14 mJ/m^2) [15], the SFE values for the 45Cr-15Co-40Ni and 45Cr-25Co-30Ni alloys are respectively higher and lower than that of the equiatomic Cr-Co-Ni alloy. The order of SFEs for the four alloys deduced by the experiment coincides with those calculated by DFT (γ_{isf}) (Fig. 10), although the prediction of the absolute value is impossible by DFT calculation.

Sets of orientation and phase (FCC and HCP) maps of deformation microstructures are shown in Fig. 11(a)-(e), respectively, for 45Cr-15Co-40Ni, 40Cr-20Co-40Ni, 45Cr-20Co-35Ni, 45Cr-25Co30Ni and 40Cr-40Co-20Ni alloys (arranged in the descending order of the calculated SFEs) deformed in tension at 77 K to failure. The observations were made at areas away from the necking part of the tensile samples. For the 45Cr-15Co-40Ni alloy (Fig. 11(a)), the viewed area is almost completely occupied by the FCC phase with twin lamellae observed in many grains. This indicates that deformation twinning contributes considerably to the plastic deformation. However, it does not exclude the existence of very thin HCP lamellae below the resolution limit. As the calculated SFE decreases, the volume fraction of the HCP phase in the lamellar form, indicative of the occurrence of ε-martensitic transformation, increases gradually from less than 1 vol. % for the 40Cr-20Co-40Ni alloy (Fig. 11(b)) to 3.5 vol. % for the 45Cr-20Co-35Ni alloy (Fig. 11(c)). For both alloys, areas occupied by twin lamellae are also observed occasionally. For 45Cr-25Co-30Ni (Fig. 11(d)) and 40Cr-40Co-20Ni alloys (Fig. 11(e)), however, the volume fraction of the HCP phase in the lamellar form increases significantly to exceed 10 %, indicating the significant contribution of ε-martensitic transformation to the plastic deformation. The variation of the volume fraction of the HCP phase is depicted in Fig. 12 as a function of the calculated SFE for these five alloys. The major deformation mode changes from deformation twinning to ε-martensitic transformation as the SFE decreases, being consistent with many previous reports [64–67]. Of significance to note is that once the volume fraction of the deformation-induced HCP phase is increased considerably as in the 45Cr-25Co-30Ni and 40Cr-40Co-20Ni alloys, the tensile ductility decreases dramatically as seen in Fig. 8. This appears to be due to the increased propensity for crack nucleation at grain boundaries and annealing twin boundaries that are impinged by deformation-induced ε-martensite laths with decreasing SFE. Fig. 13 shows the case of the 40Cr-40Co-20Ni alloys deformed in tension to failure at 77 K. The crack surrounded by ε-martensite laths is clearly observed at the grain boundaries after the tensile fracture. The decrease in tensile ductility related to the formation of deformation-induced ε-martensite laths is also observed similarly for Co-based alloys and high-Mn steels [66–68].

4. Discussion

4.1. Correlation between theoretical calculation and experimental measurement

In the present study, we used theoretically calculated MSAD and SFE values as index to predict the strength and ductility, respectively, in the ternary Cr-Co-Ni system. We further used the 0 K yield strength deduced from the temperature dependence of yield strength and tensile elongation at 77 K to evaluate the prediction. For strength, considering that all specimens used in this study have FCC single-phase microstructures with a similar grain size, the contribution of the grain boundary strengthening on the mechanical properties for all compositions is expected to be comparable. Besides, the so-called short range ordering effect, which was thought may improve the mechanical properties significantly, has been proved to have no detectable effect on either the strength or the ductility [24,25]. Thus, the difference in strength of the present Cr-Co-Ni MEAs is considered to be dominantly determined by solid solution hardening, which is expected to have a good correlation to the MSAD [1,8,9]. Theoretical calculations indicate that the MSAD increases with the increase in the Cr content and with the increase in the Ni/Co ratio at the high Cr compositions (Fig. 2(a)). This is indeed confirmed by the present experiments. A linear correlation is found between the yield strength at 0 K and MSAD (Fig. 6(b)) and the strength at 0 K increases as the Ni content increases for a given Cr content, as shown in Fig. 14(a) for the case of alloys of the 45Cr series.

On the other hand, theoretical calculations indicate that the SFE decreases with the increase in the Cr content and with the increase in the Co/Ni ratio at the high Cr compositions (Fig. 2(b)), but the tensile ductility varies in a much more complex way with respect to the variation of SFE (Fig. 8). The tensile elongation at failure increases with the decrease in SFE down to the SFE of −110 to −120 mJ/m^2 (theoretically calculated values) as expected, but it abruptly decreases once the SFE decreases below this value. The abrupt decrease in tensile ductility is confirmed to be closely related to the change in major deformation mode from deformation twinning to deformation-induced ε-martensite transformation (Figs. 11–13). This indicates that the decrease in SFE is indeed beneficial to tensile ductility as far as the major deformation mode is deformation twinning, but the further decrease in SFE that causes to change in the major deformation mode to deformation-induced ε-martensite transformation is detrimental to tensile ductility. While theoretical calculations predict that at the high Cr concentrations (such as 40Cr and 45Cr), Co-rich compositions are preferred for higher ductility due to lower SFEs, the experiments indicate that higher tensile elongations are unexpectedly obtained at Ni-rich compositions (Fig. 14(b)). The authors would like to mention that, due to instrumental restriction, we did not employ an industrial standard tensile specimens for the ductility investigation and that the elongation was deduced from the displacement of the crosshead instead with using the extensometer. Both may cause an overestimation in tensile elongation (by 15–20 % at failure as confirmed by measuring the extension of the distance between two reference points (Vickers indents) within the gage length), but the yield strength measured in this study is considered not affected by the lack of an extensometer, as reported by other researchers [69,70]. We believe that the tensile strength and ductility thus obtained can be used to confirm the correlation between the experimentally measured mechanical properties and the theoretically calculated prediction parameters, as the relative values of tensile elongation may not change.

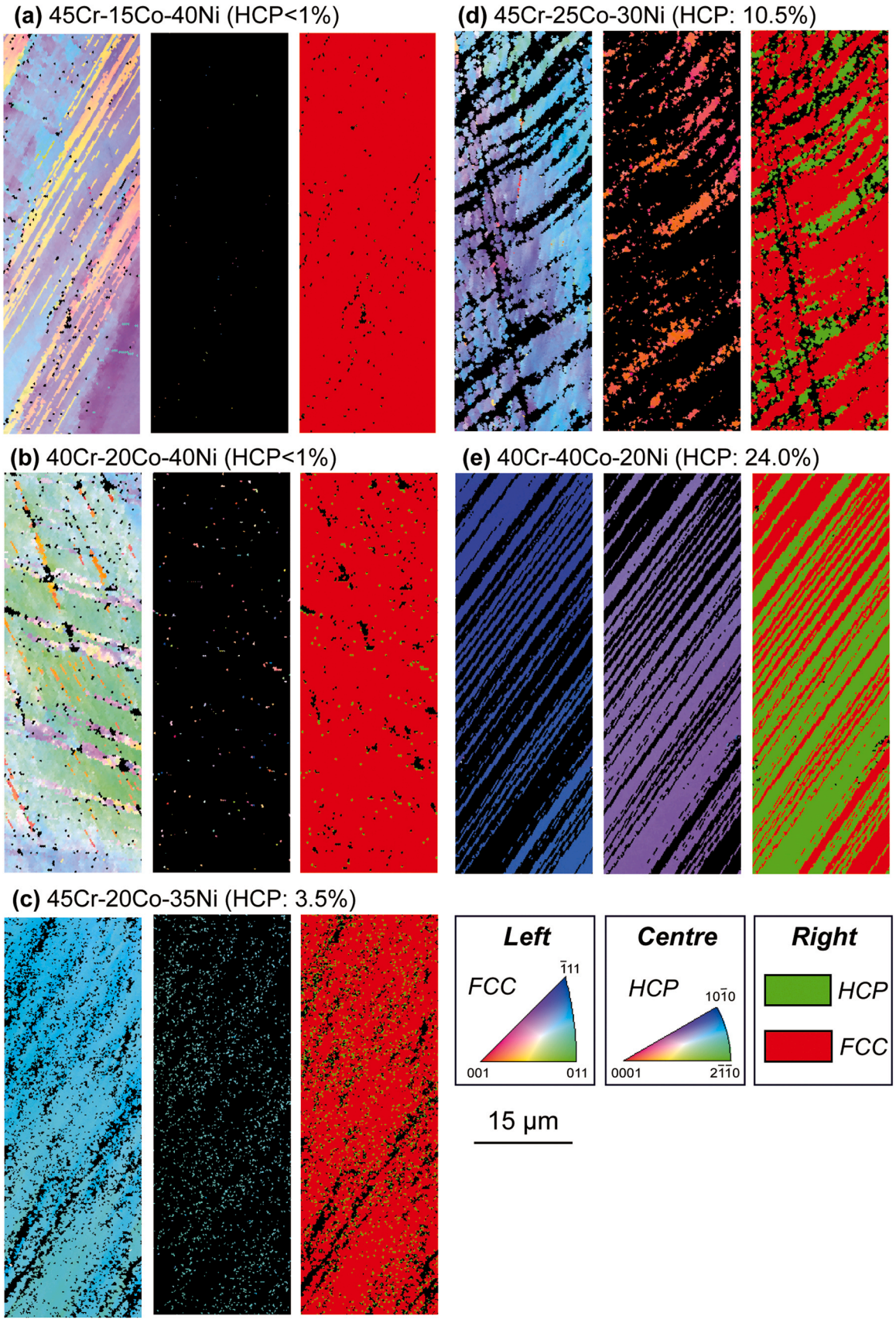

Fig. 11. Orientation map and phase (FCC and HCP) maps of deformation microstructures of (a) 45Cr-15Co-40Ni, (b) 40Cr-20Co-40Ni, (c) 45Cr-20Co-35Ni, (d) 45Cr-25Co30Ni and (e) 40Cr-40Co-20Ni alloys deformed in tension at 77 K to failure.

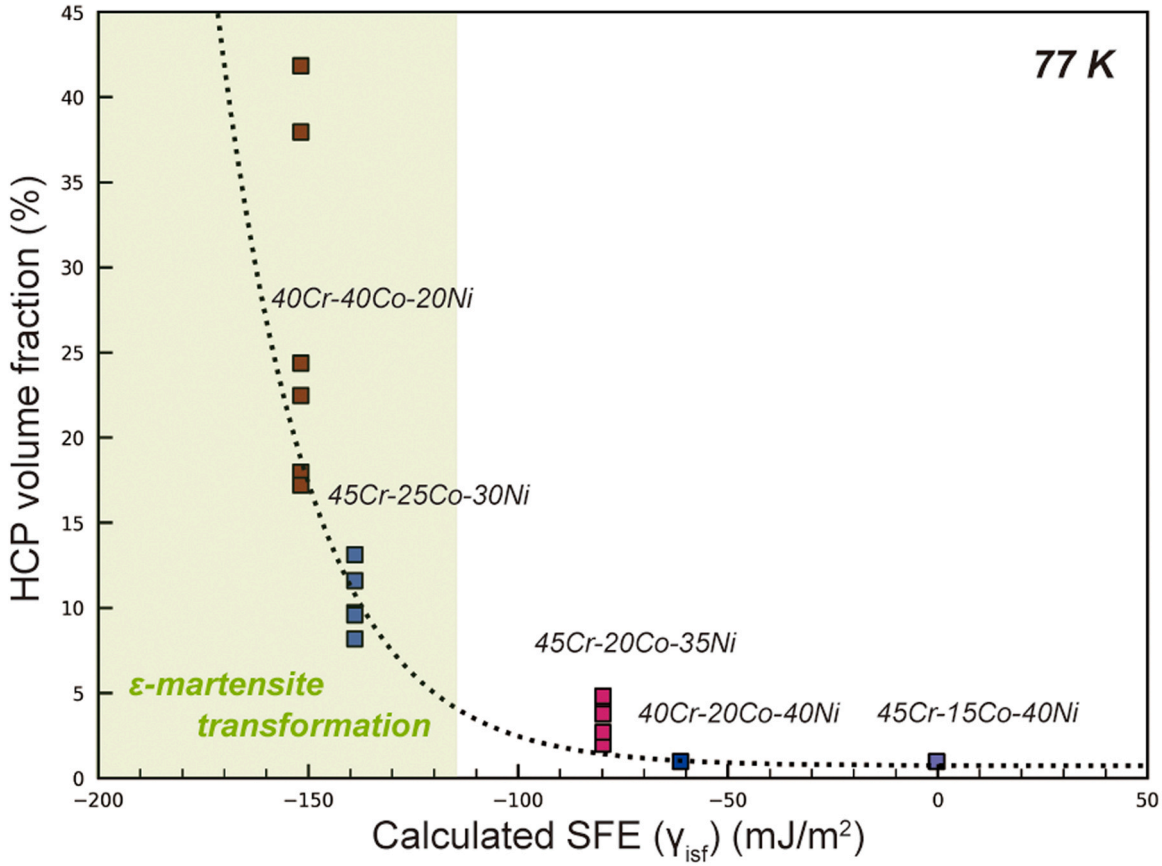

Fig. 12. Variation of the volume fraction of the deformation-induced HCP phase (in tension at 77 K) plotted as a function of theoretically calculated SFE of the five Cr-Co-Ni ternary alloys.

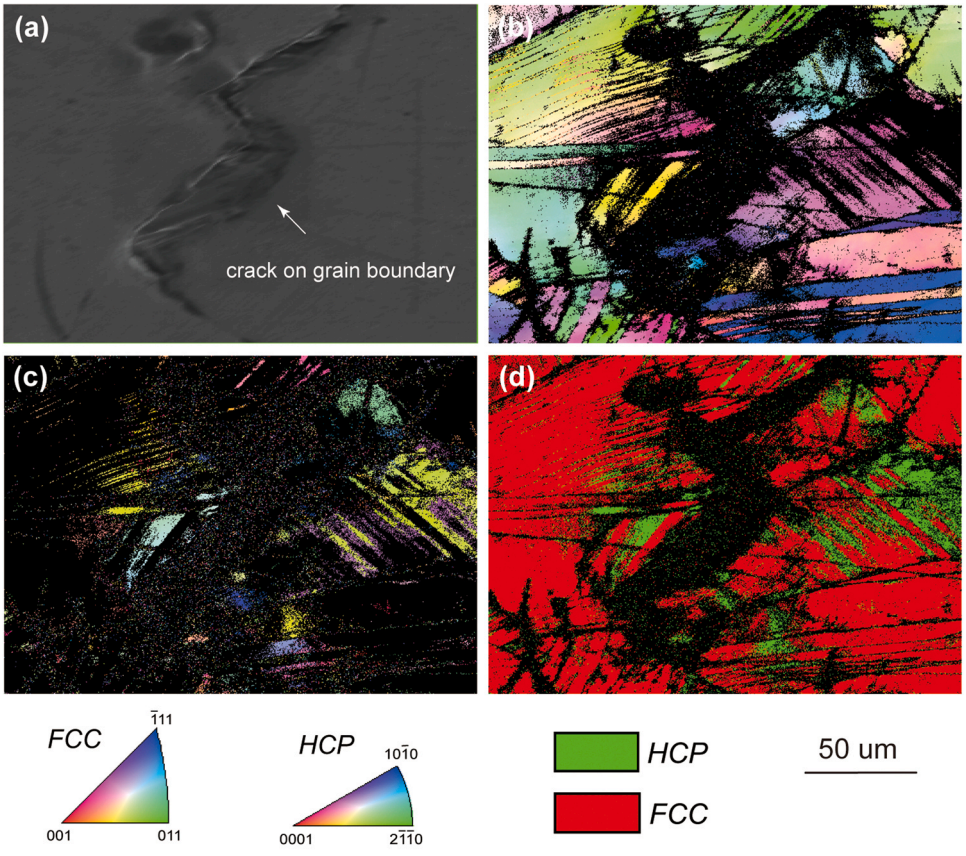

Fig. 13. Surface investigation on the crack area. (a) SEM image, orientation maps ((b) in FCC and (c) HCP phases), and (d) phase (FCC and HCP) map of the 40Cr-40Co-20Ni alloy deformed in tension at 77 K to failure.

4.2. Prediction of the composition region for simultaneous high strength and high ductility

As discussed above, in Cr-Co-Ni ternary alloys, the strength is expected to increase with increasing MSAD, whereas the ductility is believed to increase with decreasing SFE to a critical value. In other word, the MSAD parameter is expected to be as high as possible, while the SFE parameter is expected to be lower, but not too low, in order to prevent the harmful deformation-induced ε-martensite transformation. The change in the major deformation mode from deformation twinning to deformation-induced ε-martensite transformation occurs at the SFE of − 110∼− 120 mJ/m^2 in our theoretical calculation, which corresponds to 10–12 mJ/m^2 in TEM analysis (Fig. 9). The contour of SFE= −110∼− 120 mJ/m^2 is indicated as a thick line in Fig. 14(b) to indicate compositions at which an abrupt decrease in tensile ductility is expected to occur. This leads to a result that, for high strength, the higher Cr (more than 40 %) and higher Ni composition are mandatory. While for high ductility, higher Cr and higher Co compositions are preferred, but should not cross the critical line corresponding the deformation mode change.

For the above reasons, outstanding combinations of strength and ductility are obtained at compositions of a bit Ni-rich side of the Co/Ni equi-composition line at the high Cr compositions (such as 45Cr-20Co-35Ni, 45Cr-25Co-30Ni and 45Cr-15Co-40Ni) with the 45Cr-20Co-35Ni alloy being the best combination of the 0 K strength (672 MPa) and the 77 K tensile ductility (149 %). The poor ductility of the 45Cr-27.5Co-27.5Ni proposed by Coury et al. [71] as the strongest alloy may be due to the occurrence of deformation-induced ε-martensite transformation because of the too low SFE. The 45Cr-20Co-35Ni alloy, which represents the optimal combination of mechanical properties in the current study, outperforms the equiatomic Cr-Co-Ni alloy with equal grain size in terms of 0 K strength and 77 K tensile ductility by 32 % and 13 %, respectively.

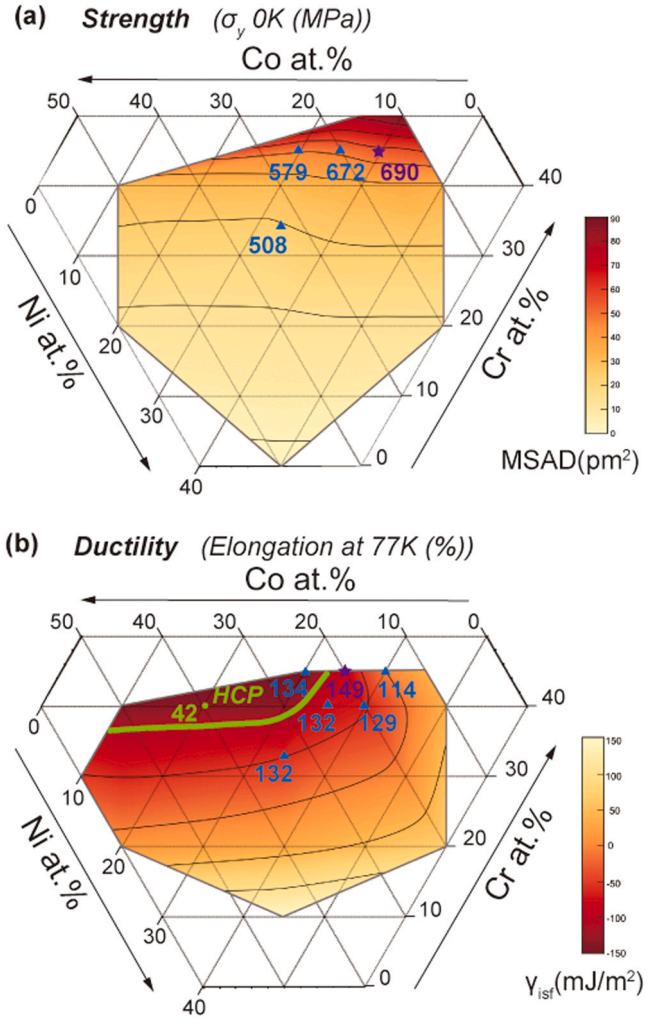

Fig. 14. (a) Experimentally-measured 0 K yield strength and (b) 77 K tensile ductility of some selected Cr-Co-Ni ternary alloys overlaid on the contour plots of theoretical calculated MSADs and SFEs, respectively.

5. Conclusions

We have attempted alloy design to achieve high strength and high ductility simultaneously for Cr-Co-Ni ternary alloys with MSAD and SFE as the respective materials parameters. The alloy design strategy has been verified by experiment through the evaluation of mechanical properties and deformation microstructures. The results obtained are summarized as follows:

(1) The MSAD is calculated to increase with the increase in the Cr content and with the increase in the Ni/Co ratio at the high Cr compositions. On the other hand, the SFE is calculated to decrease with the increase in the Cr content and with the increase in the Co/Ni ratio at the high Cr compositions. These indicate that higher Cr (more than 40 %) is mandatory for high strength and high ductility and that at such high Cr contents, Ni-rich compositions are preferred for higher strength and Co-rich compositions for higher ductility.

(2) A linear correlation is found between the yield strength at 0 K and MSAD and the strength at 0 K increases as the Ni content increases for a given Cr content. This is consistent with what is expected from the variation of MSAD. The variation of tensile ductility, on the other hand, occurs in a much more complex way than what is expected simply from the variation of SFE. The tensile elongation at failure increases with the decrease in SFE down to the SFE of 10–12 mJ/m^2 as expected, but it abruptly decreases once the SFE decreases below this value due to the change in the major deformation mode from deformation twinning to deformation-induced ε-martensite transformation.

(3) Outstanding combinations of strength and ductility are obtained at compositions of a bit Ni-rich side of the Co/Ni equi-composition line at the high Cr compositions around 45Cr-20Co-35Ni. Compared to the equiatomic Cr-Co-Ni alloy with a similar grain size, the 45Cr-20Co-35Ni alloy, the best combination alloy in the present study, exhibits 0 K strength and 77 K tensile ductility greater, respectively, by 32 % and 13 %.

CRediT authorship contribution statement

Zhi Wang: Data curation, Investigation, Software, Visualization, Writing – original draft. **Le Li**: Investigation, Writing – review & editing. **Zhenghao Chen**: Investigation, Visualization, Writing – review & editing. **Koretaka Yuge**: Methodology, Writing – review & editing. **Kyosuke Kishida**: Writing – review & editing. **Haruyuki Inui**: Supervision, Conceptualization, Methodology, Funding acquisition, Writing – review & editing. **Martin Heilmaier**: Writing – review & editing.

Data Availability

The data that has been used is confidential.

Declaration of Competing Interest

The authors declare that they have no known competing financial interests or personal relationships that could have appeared to influence the work reported in this paper.

Acknowledgments

This work was supported by Grant-in-Aids for Scientific Research on Innovative Areas on High Entropy Alloys through the grant number JP18H05450 and JP18H05451 from the Ministry of Education, Culture, Sports, Science and Technology (MEXT) of Japan, in part by JSPS KAKENHI (grant numbers JP18H05478, JP19H00824, JP19K22053, JP20K21084, JP21H01651, and JP21K14546) and JST Spring (grant number JPMJSP2110). HI and MH acknowledge the support from the Alexander von Humboldt Foundation for their cooperative research conducted under the Humboldt Fellowship of HI.

Appendix A. Supporting information

Supplementary data associated with this article can be found in the online version at doi:10.1016/j.jallcom.2023.170555.

References

[1] N.L. Okamoto, K. Yuge, K. Tanaka, H. Inui, E.P. George, Atomic displacement in the CrMnFeCoNi high-entropy alloy-a scaling factor to predict solid solution strengthening, AIP Adv. 6 (2016) 125008, , https://doi.org/10.1063/1.4971371
[2] D.B. Miracle, O.N. Senkov, A critical review of high entropy alloys and related concepts, Acta Mater. 122 (2017) 448–511, https://doi.org/10.1016/j.actamat.2016.08.081
[3] Y.Y. Zhao, T.G. Nieh, Correlation between lattice distortion and friction stress in Ni-based equiatomic alloys, Intermetallics 86 (2017) 45–50, https://doi.org/10.1016/j.intermet.2017.03.011
[4] L.R. Owen, N.G. Jones, Lattice distortions in high-entropy alloys, J. Mater. Res. 33 (2018) 2954–2969, https://doi.org/10.1557/jmr.2018.322
[5] W.G. Nöhring, W.A. Curtin, Correlation of microdistortions with misfit volumes in high entropy alloys, Scr. Mater. 168 (2019) 119–123, https://doi.org/10.1016/j.scriptamat.2019.04.012
[6] S.S. Sohn, A. Kwiatkowski Da Silva, Y. Ikeda, F. Kormann, W. Lu, W.S. Choi, B. Gault, D. Ponge, J. Neugebauer, D. Raabe, Ultrastrong medium-entropy single-phase alloys designed via severe lattice distortion, Adv. Mater. 31 (2019) 1807142, , https://doi.org/10.1002/adma.201807142
[7] Z. Li, S. Zhao, R.O. Ritchie, M.A. Meyers, Mechanical properties of high-entropy alloys with emphasis on face-centered cubic alloys, Prog. Mater. Sci. 102 (2019) 296–345, https://doi.org/10.1016/j.pmatsci.2018.12.003
[8] H. Inui, K. Kishida, L. Li, A.M. Manzoni, S. Haas, U. Glatzel, Uniaxial mechanical properties of face-centered cubic single- and multiphase high-entropy alloys, MRS Bull. (2022) 1–7, https://doi.org/10.1557/S43577-022-00280-Y
[9] Z. Fan, L. Li, Z. Chen, M. Asakura, C. Zhang, Z. Yang, H. Inui, E.P. George, Temperature-dependent yield stress of single crystals of non-equiatomic Cr-Mn-Fe-Co-Ni high-entropy alloys in the temperature range 10–1173 K, Acta Mater. 246 (2023) 118712, , https://doi.org/10.1016/j.actamat.2023.01.118712
[10] N.L. Okamoto, S. Fujimoto, Y. Kambara, M. Kawamura, Z.M.T. Chen, H. Matsunoshita, K. Tanaka, H. Inui, E.P. George, Size effect, critical resolved shear stress, stacking fault energy, and solid solution strengthening in the CrMnFeCoNi high-entropy alloy, Sci. Rep. 6 (2016) 35863, https://doi.org/10.1038/srep35863
[11] G. Laplanche, A. Kostka, C. Reinhart, J. Hunfeld, G. Eggeler, E.P. George, Reasons for the superior mechanical properties of medium-entropy CrCoNi compared to high-entropy CrMnFeCoNi, Acta Mater. 128 (2017) 292–303, https://doi.org/10.1016/j.actamat.2017.02.036
[12] Y. Wang, B. Liu, K. Yan, M. Wang, S. Kabra, Y.-L. Chiu, D. Dye, P.D. Lee, Y. Liu, B. Cai, Probing deformation mechanisms of a FeCoCrNi high-entropy alloy at 293 and 77 K using in situ neutron diffraction, Acta Mater. 154 (2018) 79–89, https://doi.org/10.1016/j.actamat.2018.05.013
[13] M. Naeem, H. He, F. Zhang, H. Huang, S. Harjo, T. Kawasaki, B. Wang, S. Lan, Z. Wu, F. Wang, Cooperative deformation in high-entropy alloys at ultralow temperatures, Sci. Adv. 6 (2020) eaax4002, https://doi.org/10.1126/sciadv.aax4002
[14] M. Kawamura, M. Asakura, N.L. Okamoto, K. Kishida, H. Inui, E.P. George, Plastic deformation of single crystals of the equiatomic Cr–Mn–Fe–Co–Ni high-entropy alloy in tension and compression from 10 K to 1273 K, Acta Mater. 203 (2021) 116454, , https://doi.org/10.1016/j.actamat.2020.10.073
[15] L. Li, Z. Chen, S. Kuroiwa, M. Ito, K. Kishida, H. Inui, E.P. George, Tensile and compressive plastic deformation behavior of medium-entropy Cr-Co-Ni single crystals from cryogenic to elevated temperatures, Int. J. Plast. 148 (2022) 103144, , https://doi.org/10.1016/J.IJPLAS.2021.103144
[16] B. Gludovatz, A. Hohenwarter, K.V.S. Thurston, H. Bei, Z. Wu, E.P. George, R.O. Ritchie, Exceptional damage-tolerance of a medium-entropy alloy CrCoNi at cryogenic temperatures, Nat. Commun. 7 (2016) 1–8, https://doi.org/10.1038/ncomms10602
[17] Z. Zhang, H. Sheng, Z. Wang, B. Gludovatz, Z. Zhang, E.P. George, Q. Yu, S.X. Mao, R.O. Ritchie, Dislocation mechanisms and 3D twin architectures generate exceptional strength-ductility-toughness combination in CrCoNi medium-entropy alloy, Nat. Commun. 8 (2017) 1–8, https://doi.org/10.1038/ncomms14390
[18] D. Liu, Q. Yu, S. Kabra, M. Jiang, P. Forna-kreutzer, R. Zhang, M. Payne, F. Walsh, B. Gludovatz, M. Asta, A.M. Minor, E.P. George, R.O. Ritchie, Exceptional fracture toughness of CrCoNi-based medium- and high-entropy alloys at 20 kelvin, Science 378 (2022) 978–983, https://doi.org/10.1126/science.abp8070
[19] F.X. Zhang, S. Zhao, K. Jin, H. Xue, G. Velisa, H. Bei, R. Huang, J.Y.P. Ko, D.C. Pagan, J.C. Neuefeind, W.J. Weber, Y. Zhang, Local structure and short-range order in a NiCoCr solid solution alloy, Phys. Rev. Lett. 118 (2017) 1–6, https://doi.org/10.1103/PhysRevLett.118.205501
[20] J. Ding, Q. Yu, M. Asta, R.O. Ritchie, Tunable stacking fault energies by tailoring local chemical order in CrCoNi medium-entropy alloys, Proc. Natl. Acad. Sci. U. S. A. 115 (2018) 8919–8924, https://doi.org/10.1073/pnas.1808660115
[21] Q.J. Li, H. Sheng, E. Ma, Strengthening in multi-principal element alloys with local-chemical-order roughened dislocation pathways, Nat. Commun. 10 (2019) 1–11, https://doi.org/10.1038/s41467-019-11464-7
[22] R. Zhang, S. Zhao, J. Ding, Y. Chong, T. Jia, C. Ophus, M. Asta, R.O. Ritchie, A.M. Minor, Short-range order and its impact on the CrCoNi medium-entropy alloy, Nature 581 (2020) 283–287, https://doi.org/10.1038/s41586-020-2275-z
[23] B. Yin, S. Yoshida, N. Tsuji, W.A. Curtin, Yield strength and misfit volumes of NiCoCr and implications for short-range-order, Nat. Commun. 11 (2020) 2507, https://doi.org/10.1038/s41467-020-16083-1
[24] L. Li, Z. Chen, S. Kuroiwa, M. Ito, K. Yuge, K. Kishida, H. Tanimoto, Y. Yu, H. Inui, E.P. George, Evolution of short-range order and its effects on the plastic deformation behavior of single crystals of the equiatomic Cr-Co-Ni medium-entropy alloy, Acta Mater. 243 (2023), https://doi.org/10.1016/j.actamat.2022.118537
[25] T. Teramoto, K. Kitasumi, R. Shimohara, Y. Ito, R. Shimizu, K. Tanaka, R. Ueji, Formation condition and effect on the early stages of plastic deformation of chemical short-range order in Cr-Co-Ni medium-entropy alloy, J. Alloy. Compd. 941 (2023) 169016, , https://doi.org/10.1016/j.jallcom.2023.01.169016
[26] F.G. Coury, K.D. Clarke, C.S. Kiminami, M.J. Kaufman, A.J. Clarke, High throughput discovery and design of strong multicomponent metallic solid solutions, Sci. Rep. 8 (2018) 1–10, https://doi.org/10.1038/s41598-018-26830-6
[27] F.G. Coury, D. Santana, Y. Guo, J. Copley, L. Otani, S. Fonseca, G. Zepon, C. Kiminami, M. Kaufman, A. Clarke, Design and in-situ characterization of a strong and ductile co-rich multicomponent alloy with transformation induced plasticity, Scr. Mater. 173 (2019) 70–74, https://doi.org/10.1016/j.scriptamat.2019.07.045
[28] S. Yoshida, T. Ikeuchi, Y. Bai, N. Tsuji, Effect of cobalt-content on mechanical properties of non-equiatomic CoCrNi medium entropy alloys, Mater. Trans. 61 (2020) 587–595, https://doi.org/10.2320/matertrans.MT-MK2019004
[29] F.G. Coury, P. Wilson, K.D. Clarke, M.J. Kaufman, A.J. Clarke, High-throughput solid solution strengthening characterization in high entropy alloys, Acta Mater. 167 (2019) 1–11, https://doi.org/10.1016/j.actamat.2019.01.029
[30] J. Yan, W. Fang, J. Huang, J. Zhang, R. Chang, X. Zhang, B. Liu, J. Feng, F. Yin, Plastic deformation mechanism of CoCrxNi medium entropy alloys, Mater. Sci. Eng. A 814 (2021) 141181, , https://doi.org/10.1016/j.msea.2021.141181
[31] D. Huang, Y. Zhuang, C. Wang, Advanced mechanical properties obtained via accurately tailoring stacking fault energy in Co-rich and Ni-depleted CoxCr33Ni67-x medium-entropy alloys, Scr. Mater. 207 (2022) 114269, , https://doi.org/10.1016/j.scriptamat.2021.114269
[32] J.B. Yang, Z.F. Zhang, Design and optimization of the composition and mechanical properties for non-equiatomic CoCrNi medium-entropy alloys, J. Mater. Sci. Technol. (2022), https://doi.org/10.1016/j.jmst.2022.07.031
[33] F.C. Puosso, G. Bertoli, F.G. Coury, A Hall–Petch study of the high toughness Cr40Co30Ni30 multi-principal element alloy, J. Mater. Res. 38 (2022) 215–227, https://doi.org/10.1557/s43578-022-00729-5
[34] G. Bertoli, L.B. Otani, A.J. Clarke, C.S. Kiminami, F.G. Coury, Hall-Petch and grain growth kinetics of the low stacking fault energy TRIP Cr40Co40Ni20 multi-principal element alloy, Appl. Phys. Lett. 119 (2021), https://doi.org/10.1063/5.0057888
[35] I. Toda-Caraballo, P.E.J. Rivera-Diaz-del-Castillo, P.E.J. Rivera-Díaz-Del-Castillo, Modelling solid solution hardening in high entropy alloys, Acta Mater. 85 (2015) 14–23, https://doi.org/10.1016/j.actamat.2014.11.014
[36] C. Varvenne, G.P.M.M. Leyson, M. Ghazisaeidi, W.A. Curtin, Solute strengthening in random alloys, Acta Mater. 124 (2017) 660–683, https://doi.org/10.1016/j.actamat.2016.09.046
[37] R. Chang, W. Fang, J. Yan, H. Yu, X. Bai, J. Li, S. Wang, S. Zheng, F. Yin, Microstructure and mechanical properties of CoCrNi-Mo medium entropy alloys: experiments and first-principle calculations, J. Mater. Sci. Technol. 62 (2021) 25–33, https://doi.org/10.1016/j.jmst.2020.04.062
[38] D. Wei, W. Gong, T. Tsuru, I. Lobzenko, X. Li, S. Harjo, T. Kawasaki, H. Do, J. Wung, C. Wagner, G. Laplanche, Y. Koizumi, H. Adachi, K. Aoyagi, A. Chiba, B. Lee, H. Seop, Si-addition contributes to overcoming the strength-ductility trade-off in high-entropy alloys, Int. J. Plast. 159 (2022) 103443, , https://doi.org/10.1016/j.ijplas.2022.103443
[39] D. Wei, L. Wang, Y. Zhang, W. Gong, T. Tsuru, I. Lobzenko, J. Jiang, S. Harjo, T. Kawasaki, J.W. Bae, W. Lu, Z. Lu, Y. Hayasaka, T. Kiguchi, N.L. Okamoto, T. Ichitsubo, H.S. Kim, T. Furuhara, E. Ma, H. Kato, Metalloid substitution elevates simultaneously the strength and ductility of face-centered-cubic high-entropy alloys, Acta Mater. 225 (2022) 117571, , https://doi.org/10.1016/J.ACTAMAT.2021.117571
[40] H. Chung, D.W. Kim, W.J. Cho, H.N. Han, Y. Ikeda, S. Ishibashi, F. Körmann, S.S. Sohn, Effect of solid-solution strengthening on deformation mechanisms and strain hardening in medium-entropy V1-xCrxCoNi alloys, J. Mater. Sci. Technol. 108 (2022) 270–280, https://doi.org/10.1016/J.JMST.2021.07.042

[41] M.L. Ali, Enhanced lattice distortion, yield strength, critical resolved shear stress, and improving mechanical properties of transition-metals doped CrCoNi medium entropy alloy, RSC Adv. 11 (2021) 23719–23724, https://doi.org/10.1039/d1ra02073k
[42] Z. Li, K.G. Pradeep, Y. Deng, D. Raabe, C.C. Tasan, Metastable high-entropy dual-phase alloys overcome the strength-ductility trade-off, Nature 534 (2016) 227–230, https://doi.org/10.1038/nature17981
[43] Z. Li, D. Raabe, Strong and ductile non-equiatomic high-entropy alloys: design, processing, microstructure, and mechanical properties, Jom 69 (2017) 2099–2106, https://doi.org/10.1007/s11837-017-2540-2
[44] S.F. Liu, Y. Wu, H.T. Wang, J.Y. He, J.B. Liu, C.X. Chen, X.J. Liu, H.T. Wang, Z.P. Lu, Stacking fault energy of face-centered-cubic high entropy alloys, Intermetallics 93 (2018) 269–273, https://doi.org/10.1016/j.intermet.2017.10.004
[45] B.C. De Cooman, Y. Estrin, S.K. Kim, Twinning-induced plasticity (TWIP) steels, Acta Mater. 142 (2018) 283–362, https://doi.org/10.1016/j.actamat.2017.06.046
[46] C. Wagner, G. Laplanche, Effects of stacking fault energy and temperature on grain boundary strengthening, intrinsic lattice strength and deformation mechanisms in CrMnFeCoNi high-entropy alloys with different Cr/Ni ratios, SSRN Electron. J. 244 (2022) 118541, , https://doi.org/10.2139/ssrn.4217267
[47] G. Kresse, J. Hafner, Ab initio molecular dynamics for liquid metals, Phys. Rev. B 47 (1993) 558–561, https://doi.org/10.1103/PhysRevB.47.558
[48] G. Kresse, J. Hafner, Ab initio molecular-dynamics simulation of the liquid-metal–amorphous-semiconductor transition in germanium, Phys. Rev. B 49 (1994) 14251–14269, https://doi.org/10.1103/PhysRevB.49.14251
[49] A. Zunger, S.-H. Wei, L.G. Ferreira, J.E. Bernard, Special quasirandom structures, Phys. Rev. Lett. 65 (1990) 353–356, https://doi.org/10.1103/PhysRevLett.65.353
[50] K. Yuge, A. Seko, Y. Koyama, F. Oba, I. Tanaka, First-principles-based phase diagram of the cubic BNC ternary system, Phys. Rev. B 77 (2008) 094121, , https://doi.org/10.1103/PhysRevB.77.094121
[51] R. Tanaka, K. Yuge, Thermodynamic stability of Mg–Y–Zn ternary alloys through first-principles, Intermetallics 72 (2016) 25–29, https://doi.org/10.1016/j.intermet.2016.01.005
[52] S. Kirkpatrick, C.D. Gelatt Jr., M.P. Vecchi, Optimization by simulated annealing, Science 220 (1983) 671–680, https://doi.org/10.1126/science.220.4598.671
[53] P.E. Blöchl, Projector augmented-wave method, Phys. Rev. B 50 (1994) 17953–17979, https://doi.org/10.1103/PhysRevB.50.17953
[54] J.P. Perdew, Y. Wang, Accurate and simple analytic representation of the electron-gas correlation energy, Phys. Rev. B 45 (1992) 13244–13249, https://doi.org/10.1103/PhysRevB.45.13244
[55] M. Methfessel, A.T. Paxton, High-precision sampling for Brillouin-zone integration in metals, Phys. Rev. B 40 (1989) 3616–3621, https://doi.org/10.1103/PhysRevB.40.3616
[56] H.J. Monkhors, J.D. Pack, Special points for Brillonin-zone integrations, Phys. Rev. B 13 (1976) 5188–5192, https://doi.org/10.1103/PhysRevB.13.5188
[57] K.P. Gupta, S.B. Rajendraprasad, A.K. Jena, R.C. Sharma, The Co-Cr-Ni system, Trans. Indian Inst. Met. 37 (1984) 699–708.
[58] Y.H. Zhang, Y. Zhuang, A. Hu, J.J. Kai, C.T. Liu, The origin of negative stacking fault energies and nano-twin formation in face-centered cubic high entropy alloys, Scr. Mater. 130 (2017) 96–99, https://doi.org/10.1016/j.scriptamat.2016.11.014
[59] S. Zhao, G.M. Stocks, Y. Zhang, Stacking fault energies of face-centered cubic concentrated solid solution alloys, Acta Mater. 134 (2017) 334–345, https://doi.org/10.1016/j.actamat.2017.05.001
[60] H. Huang, X. Li, Z. Dong, W. Li, S. Huang, D. Meng, X. Lai, T. Liu, S. Zhu, L. Vitos, Critical stress for twinning nucleation in CrCoNi-based medium and high entropy alloys, Acta Mater. 149 (2018) 388–396, https://doi.org/10.1016/j.actamat.2018.02.037
[61] E.H. Köster, A.R. Thölén, A. Howie, Stacking fault energies of Ni–Co–Cr alloys, Philos. Mag. 10 (1964) 1093–1095, https://doi.org/10.1080/14786436408225417
[62] G. Bertoli, L.B. Otani, A.J. Clarke, C.S. Kiminami, F.G. Coury, Hall-Petch and grain growth kinetics of the low stacking fault energy TRIP Cr40Co40Ni20 multi-principal element alloy, Appl. Phys. Lett. 119 (2021), https://doi.org/10.1063/5.0057888
[63] P.R. Thornton, T.E. Mitchell, P.B. Hirsch, The dependence of cross-slip on stacking-fault energy in face-centred cubic metals and alloys, Philos. Mag. 7 (1962) 1349–1369, https://doi.org/10.1080/14786436208213168
[64] P.M. Kelly, The martensite transformation in steels with low stacking fault energy, Acta Metall. 13 (1965) 635–646, https://doi.org/10.1016/0001-6160(65)90126-4
[65] M. Xu, Z. Mi, H. Li, D. Tang, H. Jiang, Deformation mechanism transition in Fe–17Mn–0.4C–0.06V TWIP steel with different strain rates, Mater. Sci. Technol. (U. K.) 34 (2018) 242–251, https://doi.org/10.1080/02670836.2017.1370157
[66] D. Wei, X. Li, W. Heng, Y. Koizumi, F. He, W.M. Choi, B.J. Lee, H.S. Kim, H. Kato, A. Chiba, Novel Co-rich high entropy alloys with superior tensile properties, Mater. Res. Lett. 7 (2019) 82–88, https://doi.org/10.1080/21663831.2018.1553803
[67] D. Wei, X. Li, J. Jiang, W. Heng, Y. Koizumi, W.M. Choi, B.J. Lee, H.S. Kim, H. Kato, A. Chiba, Novel Co-rich high performance twinning-induced plasticity (TWIP) and transformation-induced plasticity (TRIP) high-entropy alloys, Scr. Mater. 165 (2019) 39–43, https://doi.org/10.1016/j.scriptamat.2019.02.018
[68] M. Koyama, T. Sawaguchi, K. Tsuzaki, Premature fracture mechanism in an Fe-Mn-C austenitic steel, Metall. Mater. Trans. A: Phys. Metall. Mater. Sci. 43 (2012) 4063–4074, https://doi.org/10.1007/s11661-012-1220-7
[69] N. Tsuchida, S. Ueno, T. Inoue, Effect of specimen size on true stress-true strain relationship up to the plastic deformation limit in ultrafine-grained ferrite-cementite steels, Trans. JSME (Jpn.) 83 (2017), https://doi.org/10.1299/transjsme.16-00315
[70] L. Yang, L. Lu, The influence of sample thickness on the tensile properties of pure Cu with different grain sizes, Scr. Mater. 69 (2013) 242–245, https://doi.org/10.1016/j.scriptamat.2013.04.009
[71] F.G. Coury, K.D. Clarke, C.S. Kiminami, M.J. Kaufman, A.J. Clarke, High throughput discovery and design of strong multicomponent metallic solid solutions, Sci. Rep. 8 (2018) 8600, https://doi.org/10.1038/s41598-018-26830-6